THE JOURNAL OF PHYSICAL CHEMISTRY C

Article

pubs.acs.org/JPCC

A Facile Route to Coat Iron Oxide Nanoparticles with Few-Layer Graphene

R. G. Mendes,*[,†] A. Bachmatiuk,[†] A. A. El-Gendy,[‡] S. Melkhanova,[†] R. Klingeler,[§] B. Büchner,[†,∥] and M. H. Rümmeli*[,†,∥]

[†]Institute for Solid State and Materials Research Dresden e.V., PF 270116, 01171 Dresden, Germany

[‡]Nanotechnology and Nanometrology Laboratory, National Institute for Standards (NIS), Giza, Egypt

[§]Kirchhoff Institute for Physics, University of Heidelberg, Im Neuenheimer Feld 227, D-69120, Heidelberg, Germany

[∥]Department of Physics, Technische Universität Dresden, D-01062, Dresden, Germany

Supporting Information

ABSTRACT: The use of few-layer graphene coatings over nanoparticles is attractive, as it offers both long-term stability to the nanoparticles and renders them biocompatible due to the inert nature of the coating material. Moreover, graphitic coatings provide an easy platform for additional functionalization, making graphitic coated nanoparticles attractive candidates for multimodal therapeutics. Alternative strategies to coat nanoparticles often result in inhomogeneous coatings and unwanted contaminants that are hard to remove. In this work, we show the feasibility to use oleic acid as a precursor for the formation of multilayer graphene over iron oxide nanoparticles using a facile and clean route. The demonstrated graphitization process was driven by electron beam irradiation or thermal annealing. Thermal annealing leads to reduction of the iron oxide to pure iron and provides a means to tailor the magnetic properties of the multilayer graphene coated nanoparticles which are attractive as units for hyperthermia therapeutics. The graphitization process is also demonstrated over Si/SiO_2 wafers.

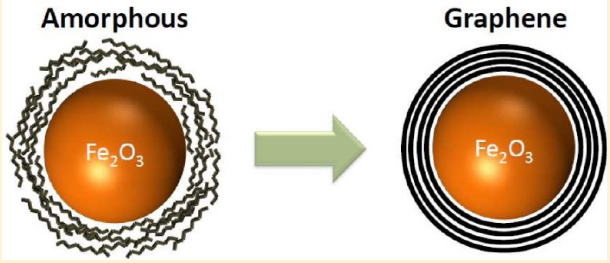

1. INTRODUCTION

A wide variety of nanoparticles (NPs) are thought to have potential for biomedical applications.[1] Among all the NPs, the class of NPs imbued with magnetic properties are of particular interest due to their potential as units for combined diagnostic and therapeutic treatment. However, challenges remain to reduce their toxicity and target them effectively to specific regions of the body.[2,3] These problems are thought to be largely due to the direct contact of the particles with an external biological environment, which can cause degradation of the NPs and result in even more toxic products.[4] A promising way to overcome this problem is to use different types of coatings that can also render these particles with new and enhanced properties.[5] Some examples include polymers,[6,7] surfactants,[8] and proteins.[9] However, often these coating materials are unstable and do not provide a homogeneous isolation of the NP surface.[10] Hence, prior to the direct biocompatibilization of NPs, it is important to use a stable and nontoxic coating that isolates the NP from the outside biological environment and ideally also serves as a platform for further functionalization. To this end, sp^2 carbon (graphene and few layer graphene) coatings have gained much interest due to their physicochemical properties that offer both covalent and noncovalent functionalization with disparate functional groups. This helps make them dispersible in a physiological environment and therefore even more biocompatible.[11,12] Moreover, the graphitic coating can carry several moieties, such as specific biomolecules that can ensure a targeted end in the organism, for example, tumors.[13,14] Finally, the graphene coating ensures the long-term stability of the core under biological environments, since they are not in contact with the external environment.[15−17]

In this contribution, we present the synthesis of iron oxide NPs using colloidal chemistry routes and describe a way to coat them with 1−12 graphene layers. Usually iron oxide NPs coated with graphene layers are fabricated using chemical vapor deposition (CVD). In addition, other techniques such as laser ablation and arc discharge are also used. A drawback of these techniques is that they yield NPs with a broad diameter distribution, and moreover, a relatively large amount of impurities are present that are difficult to remove. An alternative technique to synthesize iron oxide NPs is through colloidal chemistry. Colloidal based synthesis can yield particles with a narrow size distribution and less byproducts that can be more easily removed. In general, the byproduct is a carbonaceous material that coats the NPs, as for example shown for iron oxide NPs in ref 18. In this study, we demonstrate how this carbonaceous byproduct (oleic acid) can

Received: August 1, 2012
Revised: October 19, 2012
Published: October 22, 2012

   dx.doi.org/10.1021/jp307623h | J. Phys. Chem. C 2012, 116, 23749−23756

be used advantageously to be used as a source of carbon for the formation of graphitic layers. Moreover, we reveal the graphitization process through *in situ* transmission electron microscopy and *ex situ* investigations by annealing the NPs in dynamic vacuum at elevated temperatures. Indeed, the annealing process can alter the particle size and reduce them to iron, providing an attractive means to tailor the magnetic properties of the particles. The magnetic properties of the NPs and their potential as units for hyperthermia treatment were also investigated. Finally, the potential of oleic acid as a precursor for nanographene on alternative materials was demonstrated on Si/SiO_2 wafers.

2. METHODS

2.1. Synthesis of Iron Oxide Nanoparticles. The iron oxide nanoparticles were synthesized on the basis of the work of J. Park,[19] which is now briefly explained. A typical procedure is based on the synthesis of an iron oleate complex, which is the product of the reaction between iron chloride (III) (98%) and sodium oleate (99%) dissolved in a solvent mixture composed of ethanol, hexane, and distilled water. When heated for 4 h on a hot plate, the metal chloride and the sodium oleate react to form a metal−oleate complex (iron oleate) and sodium chloride (NaCl) (99%). The resulting mixture containing the iron oleate is then washed with distilled water to remove all the salt byproduct and separated in a separation funnel. The purified iron oleate complex presents itself in a waxy form, which is then used for the thermal decomposition in a high boiling solvent. Prior to the thermal decomposition, the purified iron−oleate complex is first dissolved in a mixture of oleic acid (90%) and 1-octadecene (90%) and heated to and then maintained at 320 °C in a reflux system for 30 min. The resulting solution, which contains the iron oxide crystals, is then cooled down to room temperature. Ethanol and acetone were used to precipitate the crystals, which were then collected using a strong magnet. The as-produced sample contains iron oxide NPs with a mean diameter of 20.3 nm (±2.6 nm). The TEM shows that the NPs are single crystals, and the X-ray diffraction (XRD) pattern suggests a maghemite phase (γ-Fe_2O_3). It is important to mention that magnetite NPs can also be present. Typically, the NPs have a coating of oleic acid over their surface which can be reduced (but not eliminated) by multiple rinsings in chloroform. This surface coating of oleic acid serves as the C rich precursor for few-layer graphene coatings on the NPs. Oleic acid has the formula $CH_3(CH_2)_7CH{=}CH\text{-}(CH_2)_7COOH$. It is classified as a monounsaturated omega-9 fatty acid and occurs naturally in various animal and vegetable fats and oils.

2.2. Growth of Graphene Nanoflakes. Few layer graphene synthesis was also conducted on silicon wafers. To achieve this, a very simple set of three steps was used to explore the formation of nanographene on Si/SiO_2 using oleic acid as the precursor. Step i: Oleic acid was spin-coated onto small pieces of Si/SiO_2 wafer (0.5×0.5 cm^2 with an oxide layer of 100 nm). Step ii: The spin-coated substrate was then covered with another clear SiO_2 wafer piece. Step iii: The sandwiched sample was annealed in a vacuum at 500 °C for 720 min.

2.3. Characterization. The samples were characterized using a variety of techniques. In order to determine the mean diameter of the NPs, a transmission electron microscope working in low voltage mode operating at 80 kV (JEOL 2010 retrofitted with two-third order Cs aberration correctors) was used. Current densities up to 100 A/cm^2 are possible. The sample was imaged in different regions, and the diameter for 100 individual particles was measured at least 4 times for each particle and then averaged. An X-ray diffractometer (model Rigaku Miniflex) was used to investigate the crystalline structure of the NPs. In addition, the obtained XRD pattern was used to estimate the average crystal size according to the Scherrer equation:[20]

$$D_{hkl} = \frac{K\cdot\lambda}{\beta\cdot\cos(\theta)}$$

where K is a shape constant factor (for spherical NPs, $K = 0.9$), λ is the X-ray wavelength (1.546 Å), β is the full width at half-maximum (fwhm) expressed in units of 2θ (radians), and θ is the Bragg angle (radians). The average diameter (D_{hkl}) of the sample was calculated to be 18.3 nm, which is in agreement with the average particle size measured using LVTEM. Table 1 summarizes the values found using the TEM (see Figure S1 in the Supporting Information) and the Scherrer equation.

Table 1. Comparison between TEM and Scherrer Mean Diameter of NPs

annealing time (min)	TEM diameter[a] (nm)	Scherrer diameter (nm)
0	19.1 (±2.6)	18.3 (±9.2)
15	18.5 (±2.4)	14.6 (±7.1)
60	27.9 (±2.5)	21.0 (±7.9)
720	33.8 (±2.9)	23.2 (±5.2)

[a]The TEM diameter shown is only from the iron oxide core. In order to have the total particle diameter, one should add a value of 2.5 nm average coating to these values (see Figure S2 in the Supporting Information).

The presence of sp^2 carbon was studied using Raman spectroscopy (model Thermo Scientific DXR, laser λ = 532 nm). Table 1 summarizes the results obtained by TEM and the Scherrer equation. To examine the different nanoparticle samples, they were pressed on Si/SiO_2 wafers. The few-layer graphene nanoflakes were synthesized on the Si/SiO_2 wafers and therefore studied directly. The heating experiments were performed in purpose built equipment with an operating frequency of 60 Hz. The samples were dispersed in an aqueous solution using a tip sonicator with a concentration of 5 mg/mL and measured over 4 min. Finally, the atomic force microscope (AFM model Digital Instruments Veeco, NanoScope IIIa) was used (in tapping mode) to measure the topographic features of the graphene nanoflakes and extract the average diameter and height (number of layers) of the nanoflakes.

3. RESULTS AND DISCUSSION

3.1. *In Situ* Graphitization of Oleic Acid on Iron Oxide NPs. Colloidal chemistry is an ideal approach with which to synthesize iron oxide nanoparticles with a well-defined diameter distribution.[19,21] One of the drawbacks of the technique is the fact that some residual reactant material always remains as a coating on the produced nanoparticles. In order to use this coating advantageously, we decided to explore the possibility of using it as a carbon source to form a graphitic coating. Graphene of few-layer graphene coatings is stable, is impermeable, and provides a wider spectrum of possibilities for additional functionalization.[16,22] In this study, we demonstrate two graphitization approaches, namely, electron beam driven graphitization *in situ* in a low voltage C_s aberration corrected transmission electron microscope (LVTEM) and

dx.doi.org/10.1021/jp307623h | J. Phys. Chem. C 2012, 116, 23749−23756

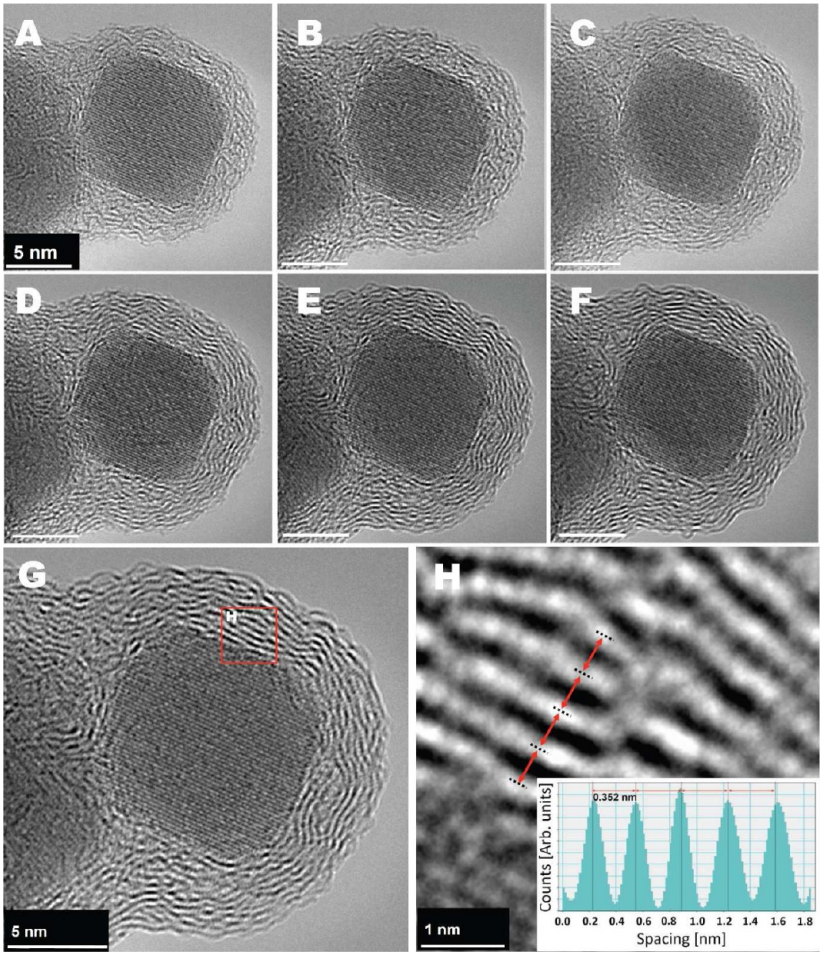

Figure 1. Panels A–F show the stepwise *in situ* graphitization of oleic acid coatings on iron oxide nanoparticles in LVTEM under electron irradiation. The time elapsed between panels A and F corresponds to an electron beam exposure of 3.5 min. Panel G shows a higher magnification of the particle in panel F with a fully graphitized coating particle after electron beam irradiation. Panel H shows a zoomed area from panel G depicting the spacing between the shells (0.35 nm). The spacing corresponds to multilayer graphene coating.

thermal driven graphitization under dynamic vacuum. We first discuss graphene layer formation of oleic acid coated iron oxide nanoparticles through an *in situ* investigation in which individual iron oxide NPs coated with oleic acid are exposed to an 80 keV LVTEM electron beam. In general, carbon based materials are sensitive to a variety of irradiation effects, namely, electronic excitations and radiolysis, knock-on displacements, and radiation induced diffusion.[23] These processes enable carbon based materials to decompose or crack, forming amorphous carbon. Exposure of amorphous carbon to the electron beam leads to the formation of sp^2 carbon, usually in the form of carbon onions if the amorphous carbon is freestanding.[24] Typically this is achieved with acceleration voltages above 100 keV; however, we have recently shown this is also possible using acceleration voltages of 80 kV.[25] The graphitization process is generally accepted to occur through radiation induced diffusion[26] which can be thought of qualitatively to be similar to thermal diffusion.

Figure 1A–F shows a series of consecutive images of the *in situ* graphitization of oleic acid coatings. In panel A, an iron oxide initially coated with oleic acid is seen. In consecutive frames, the coating thickness is seen to increase from ~2.9 to ~3.5 nm; moreover, the coating is seen to form into a layered structure with the layers forming parallel to the surface of the NP (see panel G). The layers look much like graphene layers and have an interlayer spacing of 0.35 nm which is commensurate with graphene layers (panel H). The fact the layers form parallel to the core nanoparticle surface rather than form carbon onions is attributed to van der Waals forces helping drive planar graphitization in keeping with a recent study of ours.[25]

We also observed that there is a relationship between the thickness of the fatty acid layer and the number of layers that can be formed. Panels A–F in Figure 2 show three different NPs with different thicknesses of their initial oleic acid outer coating (panels A, C, and E) and their corresponding graphitic coating (panels B, D, and F). The oleic acid coating thickness is easily controlled in the post production stage by repeated washing in chloroform. The greater the number of washing steps, the thinner the oleic acid coating is. However, a threshold is reached in which a very thin surface layer always remains, presumably because of strong van der Waals interactions and possibly chemical bonding to surface atoms, although this latter scenario is less likely. The controlled oleic acid coating varies from 0.7 to 4 nm. These oleic acid coatings result in graphene layer coatings ranging from 1 to 2 graphene layers through around 12 layers. The reaction time to form graphene layers on the surface of the NPs increases as the oleic acid coating thickness increases and is presumably related to diffusion lengths of C species.

dx.doi.org/10.1021/jp307623h | *J. Phys. Chem. C* 2012, 116, 23749–23756

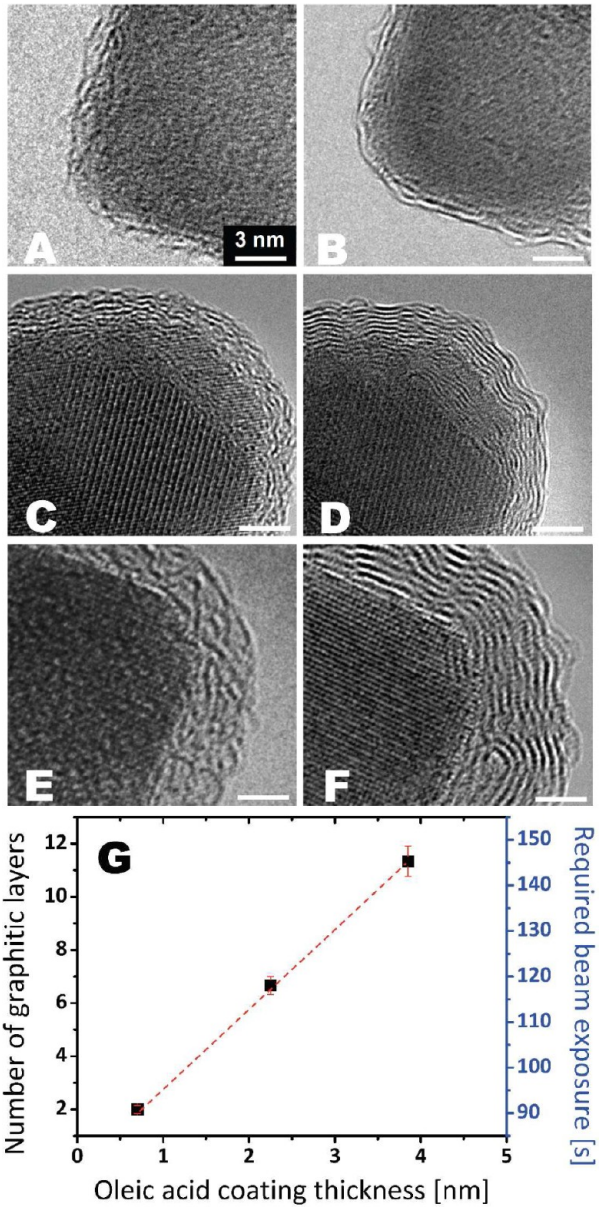

Figure 2. Examples of three different oleic acid thickness coating iron oxide particles after minimal (panels A, C, and E) and extended (B, D, and F) electron irradiation, respectively. Panel G shows the resultant number of graphene layers (after electron irradiation) and the irradiation time for full graphitization with respect to the initial oleic acid coating thickness. The dashed line serves as a guide to the eye.

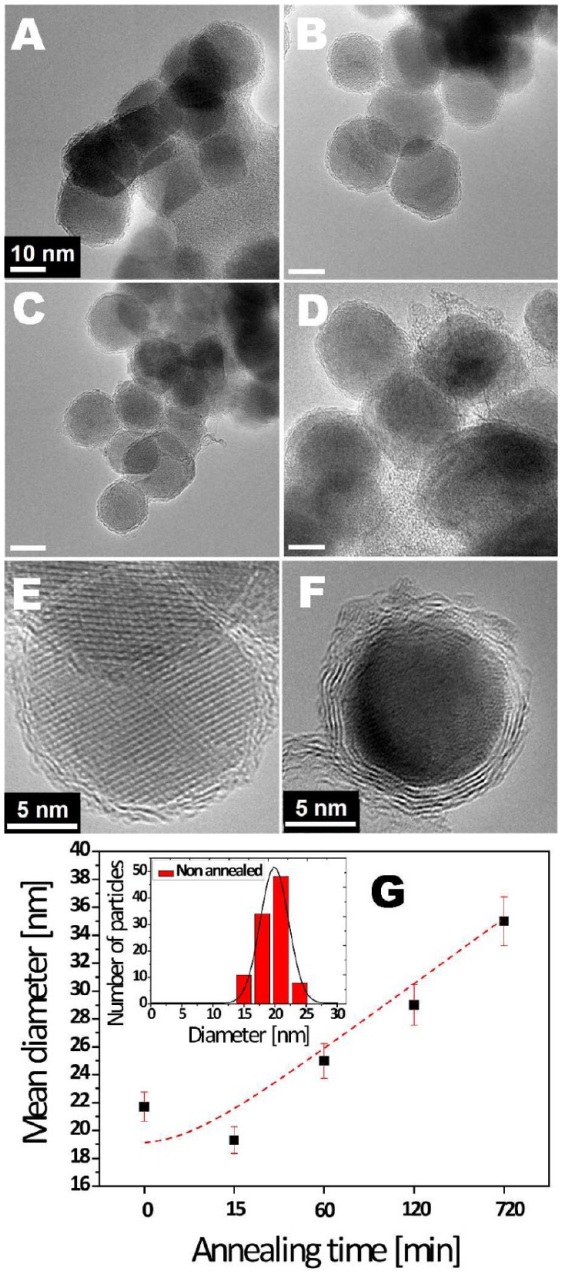

Figure 3. Panels A–E show the nanoparticles after different annealing periods (0, 15, 60, 120, and 720 min, respectively). Panels E and F show graphitic layers around the nanoparticles after thermal annealing. The annealing period for the nanoparticles was 60 and 720 min, respectively. Panel G shows the change in particle mean diameter with respect to annealing time. The dashed curve serves as a guide to the eye.

3.2. Bulk Graphitization of Oleic Acid on Iron Oxide NPs. While the *in situ* LVTEM graphitization route is interesting, it is not practical for the large scale production of graphitic coated NPs. To overcome this issue, we explored the potential of annealing the samples under high vacuum ($\sim 10^{-6}$ mbar). The samples were annealed at 500 °C for a variety of different time intervals, 15, 45, 60, 120, and 720 min. LVTEM investigations were implemented to investigate how the annealing procedure alters the coating and morphology of the particles. Typical examples are presented in Figure 3. Generally, the mean diameter of the particles increases with increasing annealing time, as illustrated in the graph shown in panel G of Figure 3. The increase in nanoparticle size is probably due to sintering.[27] The mean diameter of the NPs was estimated from TEM micrographs for at least 100 particles. In addition, the surface of the particles shows few-layer graphene, even after 15 min of annealing. Analysis of the interlayer spacing of the graphitic coating from thermally annealed samples did not differ from the measured *in situ* value, which further suggests that the parameters chosen to anneal the samples were sufficient to reproduce the results obtained in the *in situ* study. Some examples are shown in panels E and F of Figure 3.

Raman spectroscopy is a powerful technique to identify sp^2 carbon, especially through the first order peaks around 1350 and 1600 cm^{-1}, which are termed the D and G bands,

dx.doi.org/10.1021/jp307623h | J. Phys. Chem. C 2012, 116, 23749–23756

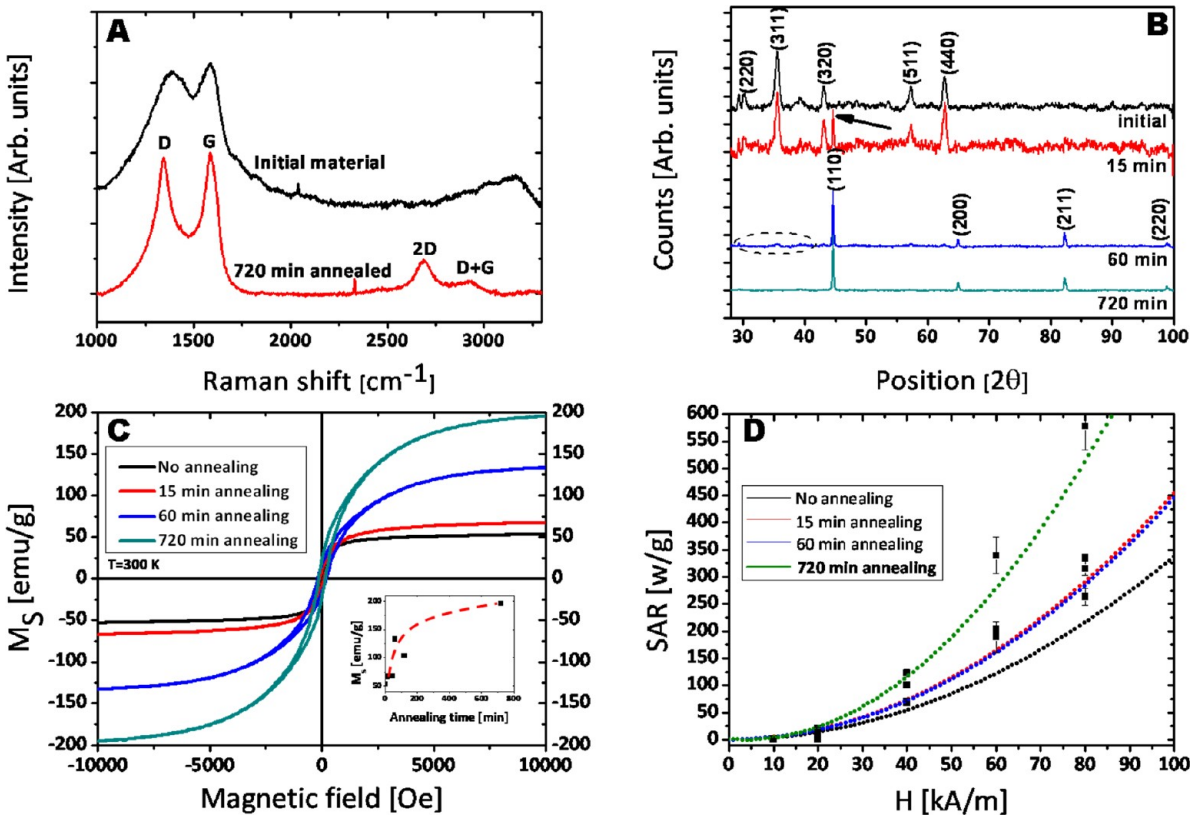

Figure 4. Panel A depicts the Raman spectra for the starting iron oxide nanoparticles and particles after thermal annealing for 720 min. Panel B shows the XRD spectra for the corresponding samples used in part A. It shows that already after 15 min of annealing some structural changes start, which are depicted by the arrow. The dashed circle suggests that after 60 min of annealing there might have some iron oxide left in the sample, as some peaks corresponding to maghemite can be seen, as also observed in the analysis of the crystalline lattice of individual particles (see Figure S4 in the Supporting Information). A magnified region highlighting the greatest changes is available in Figure S5 in the Supporting Information. Panel C shows the hysteresis curves for the samples after various annealing times. Inset: maximum M_s for each sample versus annealing time (the curve is a guide to the eye). Panel D provides the specific absorption rate (SAR) for different field strengths for the various annealed samples.

respectively. The D band arises due to breathing modes of sp^2 atoms in rings but is only active when symmetry is broken (e.g., due to a defect) due to its peculiar selection rules, and the G band arises through bond stretching of all sp^2 carbon pairs in both rings and chains.[28] The intensity ratio of the D/G modes is often used as an indicator of how crystalline the graphitic material is. Thus, it is of interest to use Raman spectroscopy to investigate our samples as a tool to help elucidate the graphitization of the oleic acid coating on our iron oxide nanoparticles. To minimize any graphitization by the excitation laser, very low laser powers (<3 mW) were used along with short collection times. The D/G intensities ratio relative to the peak area for the pristine sample (oleic acid coating) was ca. 3.5, while for the annealed samples it reduced to between 1 and 2, indicating improved crystallization. Moreover, the D and G modes were more defined, as illustrated in Figure 4A. These changes in the D/G modes are concomitant with the graphitization of the fatty acid coating.

X-ray diffraction (XRD) was used to indicate if any structural changes had occurred for the core particles. After 15 min, little to no changes are observed. For longer annealing periods, new peaks begin to emerge and old peaks diminish such that by 720 min the XRD pattern no longer matches iron oxide but matches that of pure iron (see panel B in Figure 4). This tells us the iron oxide nanoparticles chemically reduce with the annealing process. Presumably the oxygen leaves by forming carbon monoxide or dioxide species. No evidence for iron carbide was observed. To further confirm the XRD data, analysis of the crystalline lattice from TEM data was conducted (see Figure S4 in the Supporting Information). The data correlated very well with the XRD findings.

The gradual change in phase of the nanoparticles from iron oxide to iron is also visible in the magnetization data. Panel C in Figure 4 shows the magnetization curves, $M(H)$, at 300 K. Only a small change in the saturation magnetization is observed for the sample annealed for 15 min as compared to the pristine sample (from 50 to 65 emu/g). However, for the samples annealed for 60 and 720 min, the saturation magnetization goes up to 130 and 200 emu/g, respectively. In addition, there is an increase in the coercivity with annealing time which may be both due to an increase in particle size as observed in the LVTEM studies and a reduction of the iron oxide cores to Fe. This increase in the coercivity (H_c) with respect to the annealing time varies from 22 Oe in the as-synthesized particles to around 200 Oe in the 720 min annealed samples. In the literature, the coercivity values of Fe nanoparticles with the same size diameter range have been reported to vary dramatically between samples.[29,30] The reason for these differences in coercivity is not clear, but we suspect that the synthesis route or the annealing process could lead to different impurities and/or Fe ratios, leading to samples with different H_c values. This has already been observed in Fe-filled carbon nanotubes[31] and composite NPs.[32]

dx.doi.org/10.1021/jp307623h | J. Phys. Chem. C 2012, 116, 23749−23756

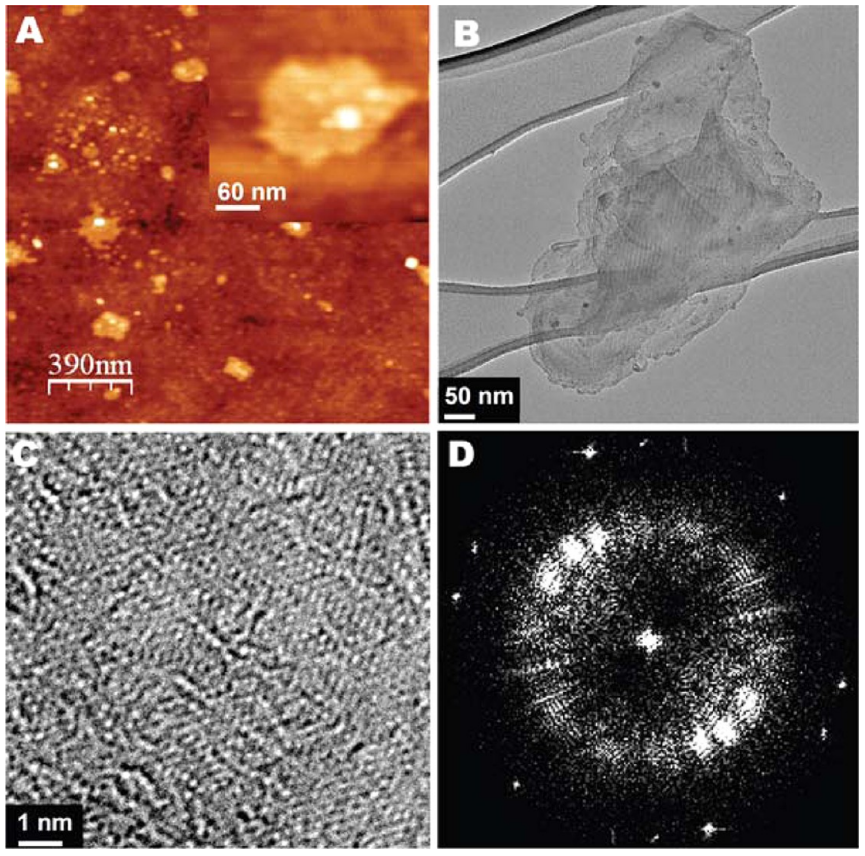

Figure 5. Panel A shows AFM images of few-layer graphene flakes residing on Si/SiO_2. The inset shows a higher magnification of a single flake. Panel B shows a LVTEM image of a flake. Panel C shows a higher magnification of a flake. The Moiré pattern indicates the multi layer graphene is turbostratic. Panel D shows the Fourier domain (from panel C) multiple sets of hexagonal reflexes corroborate rotational stacking disorder, *viz.* turbostratic few layer graphene.

One can extrapolate the ratio of magnetic material to nonmagnetic material from the saturation magnetization data. For the pristine material, one obtains a mass percentage of 72% for γ-Fe_2O_3 (with bulk $M_{S(\gamma\text{-}Fe_2O_3)}$ = 74 emu/g), while the rest is nonmagnetic, i.e., diamagnetic organic material (C) or, e.g., a small amount of α-Fe_2O_3 not detected in the XRD data. For samples annealed for 720 min, a pure Fe core is obtained as indicated from the XRD data. In addition to the chemical reduction of iron oxide with annealing, the relative amount of nonmagnetic materials in the sample also decreases, since for the annealed sample one extracts 94% mass of Fe and 6% of carbon (with bulk $M_{S(Fe)}$ = 214 emu/g).[33] For intermediate annealing levels, only rough trends can be deduced from the magnetization data, since the core does not consist of a single pure phase (only partial chemical reduction has occurred). Crudely, if one assumes 28% of the mass as C, a saturation magnetization of 133 emu/g implies 30% of Fe and 42% of γ-Fe_2O_3, which is consistent with the XRD pattern. Less carbon would imply more γ-Fe_2O_3.

The magnetization curves shown in Figure 4C imply that at least a part of the pristine particles are blocked at room temperature, which is in keeping with the critical blocking radius at 300 K occurring near that of the mean particle size for the pristine sample.[34] Upon annealing, the material converts to pure iron which exhibits a slightly higher anisotropy, which again agrees with the observation of increasing H_C. This implies that even after 15 min of annealing there is already a significant change in the core material. Concomitantly, however, there seems to be a general trend of slightly increasing core diameters which also would yield an increase of H_C in this size range, so that no clear quantitative estimates can be made.

The change in phase from iron oxide to pure iron in essence provides a means to tailor the magnetization saturation which can be attractive for hyperthermia treatment, since higher saturation magnetization translates to more efficient heating. In short, in hyperthermia treatment, magnetic nanoparticles subjected to an alternating magnetic (AC) field produce heat that may be related to several physical mechanisms. In ferromagnetic particles, the magnetization reversal is usually described by the hysteresis loop and the heating is caused by hysteresis losses.[35,36] In superparamagnetic particles, relaxation losses may be associated with rotation of the particle itself. Both the Brownian and Néel relaxation lead to a dissipation of energy which leads to heating of the local environment.

In hyperthermia, the idea is to use this heat (from both Brownian and Néel relaxation) to destroy cancer cells. Cancer cells are vulnerable to heat, so if magnetic nanoparticles are attached or taken up by cancer cells and then exposed to an alternating magnetic field, the cancer cells, which do not have the ability to endure the damaging effects of increased heat levels, will eventually die. The power dissipated by magnetic materials while under the influence of an alternating magnetic field is known as the specific absorption rate (SAR) and is expressed as power per unit mass (W/g).[37,38] In short

$$\mathrm{SAR} = \frac{c}{m_{\mathrm{act}}}\left(\frac{\mathrm{d}T}{\mathrm{d}t}\right)_{t\to 0}$$

where c is the specific heat capacity, which in the case of water is $c = 4.118\ \mathrm{J\ g^{-1}\ K^{-1}}$, and m_{act} is the mass of magnetically active material. To evaluate the hyperthermia potential of our nanoparticles, they were dispersed in an aqueous solution of 5 mg/mL and then subjected to an alternating magnetic field varying from 10 to 80 kA/m. The results are shown in Figure 4D. The data shows an increased SAR for the annealed samples relative to the pristine samples. Notably the samples prepared by annealing for 720 min heated the solution from room temperature to 50 °C in under 2 min for an alternating magnetic field of 80 kA/m (see Figure S3 in the Supporting Information).

In order to compare the results quantitatively with literature data, we normalize the data in Figure 4D to the mass of the magnetic core material only as determined by the magnetization study. For the pristine and fully reduced samples, we find SAR = 262 $\mathrm{W/g_{\gamma\text{-}Fe_2O_3}}$ (SAR normalized to the total mass = 210 $\mathrm{W/g_{\gamma\text{-}Fe_2O_3@C}}$) and 566 $\mathrm{W/g_{Fe}}$ ($\mathrm{SAR_{total}}$ = 520 $\mathrm{W/g_{Fe@C}}$), at H = 80 kA/m, respectively. For comparison, a recent study on commercial Fe@C nanoparticles with an average diameter of 25 nm was shown to have a SAR value up to 240 $\mathrm{W/g_{Fe@C}}$.[30] Reported SAR values of Co@C and Ni@C synthesized using a chemical vapor deposition (CVD) route were 162 and 131 W/g, respectively. In essence, these published values for Fe, Co, and Ni coated with carbon are comparable to our pristine material. However, our fully reduced sample exhibits a SAR value twice as good.

We also calculated the intrinsic loss power (ILP)[39] for the samples given by

$$\mathrm{ILP} = \frac{\mathrm{SAR}}{H^2 f}$$

where H is the alternating magnetic field and f is the AC field frequency, which in our case is 120 kHz. This yields $\mathrm{ILP_{\gamma\text{-}Fe_2O_3}} \sim 3.41 \times 10^{-4}\ \mathrm{nH{\cdot}m^2}$ and $\mathrm{ILP_{Fe}} \sim 7.36 \times 10^{-4}\ \mathrm{nH\ m^2/g_{Fe}}$ for the pristine and fully reduced samples, respectively. These values compare favorably with results from another recent study on Co@C with 57% mass of Co and a mean core size of 9 nm from which an $\mathrm{ILP_{Co@C}}$ of $\sim 3 \times 10^{-4}\ \mathrm{nH\ m^2/g_{Co@C}}$ ($\mathrm{ILP_{Co}} \sim 5.3 \times 10^{-4}\ \mathrm{nH\ m^2/g_{Co}}$) was obtained.[40]

The data highlight the potential to tailor the magnetic performance of iron oxide nanoparticles coated with few-layer graphene layers by chemical reduction through annealing. Moreover, the magnetic data compare favorably with other Fe@C, Co@C, and Ni@C samples discussed in the literature.

3.3. Graphitization of Oleic Acid on a $\mathrm{Si/SiO_2}$ Substrate. In order to further investigate the graphitization potential of oleic acid on alternative materials, a simple experiment was conducted. First, small pieces (5 mm × 5 mm) of clean $\mathrm{Si/SiO_2}$ wafers were spin-coated with oleic acid and annealed in a high vacuum at 500 °C for 720 min. Annealing experiments were conducted two ways. In the first, a single wafer was annealed and in the second experiment a second $\mathrm{Si/SiO_2}$ wafer was placed face down on the first wafer so as to sandwich the oleic acid film between the two $\mathrm{SiO_2}$ faces of the wafers. In the first experiment, no evidence for $\mathrm{sp^2}$ carbon was observed from atomic force microscopy (AFM) and Raman spectroscopy investigations. Presumably the oleic acid decomposes and desorbs from the surface. In the second type of experiments, Raman spectroscopy showed the presence of $\mathrm{sp^2}$ carbon (see Figure S1 in the Supporting Information). AFM showed the presence of flakes on the surface, indicating that large area graphitization does not occur but rather small domains form (see Figure 5A). The domain diameters range from 100 to 250 nm and their heights range from 1.5 to 2.5 nm, which in terms of the number of graphitic layers (assuming an interlayer spacing of 0.35 nm) is 4−7 layers. The average diameter and height were 164 and 2.0 nm (5−6 layers), respectively (see Figure S6 in the Supporting Information). To confirm the nature of the flakes, they were transferred on to Lacey carbon TEM grids and studies in LVTEM. The LVTEM studies confirmed the presences of flakes (e.g., Figure 5B). Closer examination showed Moiré patterns indicating the graphitic layers are turbostratic (Figure 5C). Looking at the Fourier domain shows multiple sets of hexagonal reflex spots confirming the presence rotational stacking faults between the graphene layers.[41] The Raman spectrum of the sample showed the characteristic D and G modes confirming the presence of $\mathrm{sp^2}$ carbon (see Figure S7 in the Supporting Information). The spacing corresponds to the graphene lattice constant, again confirming the formation of few layer graphene islands.

4. CONCLUSION

To summarize, the potential of converting oleic acid coatings on iron oxide nanoparticles into $\mathrm{sp^2}$ carbon has been successfully demonstrated. The graphitization process was shown both *in situ* and *ex situ* using either electron irradiation or thermal annealing, respectively. The data show a direct correlation between the initial oleic acid coating and the resultant number of graphene layers coating the particles. Thermal annealing reduces the iron oxide toward pure iron, and the particles coalesce, leading to larger average particles sizes. Both of these aspects lead to enhanced magnetic properties and thus provide a means to tailor the magnetic properties. The magnetic properties compare very favorably against similar nanoparticles discussed in the literature. The potential of the few-layer graphene coated particles for hyperthermia was demonstrated through specific absorption rate studies. The graphitization of oleic acid was also shown on $\mathrm{Si/SiO_2}$ wafers. By sandwiching an oleic acid film in between two $\mathrm{Si/SO_2}$ wafers, small few layer graphene flakes consisting of 4−7 layers could be formed by simply annealing in a high vacuum.

■ ASSOCIATED CONTENT

Ⓢ Supporting Information

Histograms showing particle size distribution. Heating measurements showing temperature increase at different external magnetic fields. Fourier transform of particles for different annealing times mentioned in the text. XRD information. Histograms of graphene nanoflake height and diameter measured by AFM. Typical Raman spectrum of graphene nanoflakes. This material is available free of charge via the Internet at http://pubs.acs.org.

■ AUTHOR INFORMATION

Corresponding Author

*E-mail: m.ruemmeli@ifw-dresden.de.

Notes

The authors declare no competing financial interest.

■ ACKNOWLEDGMENTS

R.G.M. thanks the DFG (RU1540/8-1), A.B. the Alexander von Humboldt and BMBF. S.M. thanks the IFF. M.H.R. thanks the EU (ECEMP) and the Freistaat Sachsen.

■ REFERENCES

(1) Hao, R.; Xing, R.; Xu, Z.; Hou, Y.; Gao, S.; Sun, S.; Hao, R.; Xing, R. *Adv. Mater.* **2010**, *22* (25), 2729−2742.
(2) Krol, S. *J. Controlled Release* **2012**, DOI: 10.1016/j.jconrel.2012.04.044.
(3) Di Gioacchino, M.; Verna, N.; Gornati, R.; Sabbioni, E.; Bernardini, G. *Nanotoxicity*; John Wiley & Sons Ltd: Chichester, U.K., 2009.
(4) Faddel, B.; Garcia-Bennett, A. E. *Adv. Drug Delivery Rev.* **2010**, *62* (3), 362−374.
(5) Mout, R.; Moyano, D. F.; Rana, S.; Rotello, V. M. *Chem. Soc. Rev.* **2012**, *41*, 2539−2544.
(6) Neoh, K. G.; Kang, E. T. *Polym. Chem.* **2011**, *2*, 747−759.
(7) Karakoti, A. S.; Das, S.; Thevuthasan, S.; Seal, S. *Angew. Chem., Int. Ed.* **2011**, *50*, 1980−1994.
(8) Park, S.; Kim, H.; Kim, W. J.; Yoo, H. S. *Int. J. Pharm.* **2012**, *424*, 107−114.
(9) Garcia-Bennett, A.; Nees, M.; Faddel, B. *Biochem. Pharmacol.* **2011**, *81*, 976−984.
(10) Mullen, D. G.; McNerny, D. Q.; Holl, M. M. B.; Baker, J. R. *Multifunctional Nanoparticles for Drug Delivery Applications*; Springer: Princeton, NJ, 2012.
(11) Tasis, D.; Tagmatarchis, N.; Bianco, A.; Prato, M. *Chem. Rev.* **2006**, *106*, 1105−1136.
(12) Ji, S.-R.; Liu, C.; Zhang, B.; Yang, F.; Xu, J.; Long, J.; Jin, C.; Fu, D.-L.; Ni, Q.-X.; Yu, X.-J. *Biochim. Biophys. Acta* **2010**, *1806*, 29−35.
(13) Liu, Z.; Robinson, J. T.; Sun, X.; Dai, H. *J. Am. Chem. Soc.* **2008**, *130*, 10876−10877.
(14) Zhang, L.; Xia, J.; Zhao, Q.; Liu, L.; Zhang, Z. *Small* **2010**, *6* (4), 537−544.
(15) Klingeler, R.; Hampel, S.; Büchner, B. Carbon nanotube based biomedical agents for heating, temperature sensoring and drug delivery. *Int. J. Hyperthermia* **2008**, *24*, 496−505.
(16) Leonhardt, A.; et al. *Chem. Vap. Deposition* **2006**, *12*, 380−387.
(17) Mueller, C.; Leonhardt, A.; Kutz, M. C.; Büchner, B.; Reuther, H. *J. Phys. Chem. C* **2009**, *113* (7), 2736−2740.
(18) Chen, Z. P.; Xu, Z.; Zhang, Y.; Gu, N. *Nanoscale Res. Lett.* **2009**, *4*, 204−209.
(19) Park, J.; An, K.; Park, J.-G.; Noh, H.-J.; Kim, J.-Y; Par, J.-H.; Hwang, N.-M.; Hyeon, T. *Nat. Mater.* **2004**, *3*, 891−895.
(20) Patterson, A. L. *Phys. Rev.* **1939**, *56*, 978−982.
(21) Brownstein, L. M.; Huang, X.; Retrum, J.; Schmucker, S.; Pink, M.; Stein, B. D.; Dragnea, B. *Chem. Mater.* **2007**, *19*, 3624−3632.
(22) Leonhardt, A.; Ritschel, A.; Kozhuharova, R.; Graff, A.; Muhl, T.; Huhle, R.; Monch, I.; Elefant, D.; Schneider, C. *Diamond Relat. Mater.* **2003**, *12*, 790−793.
(23) Banhart, F. *Rep. Prog. Phys.* **1999**, *62*, 1181−1221.
(24) Yajima, A.; Abe, S.; Fuse, T.; Mera, Y.; Maeda, K.; Suzuki, K. *Mol. Cryst. Liq. Cryst.* **2002**, *388*, 561−565.
(25) Börrnert, F.; Avdoshenko, S. M.; Bachmatiuk, A.; Ibrahim, I.; Büchner, B.; Cuniberti, G.; Rümmeli, M. *Adv. Mater.* **2012**, *24*, 5630−5635.
(26) Seeger, A. *Philos. Mag.* **1974**, *30*, 417−422.
(27) Park, J.-N.; Zhang, P.; Hu, Y.-S.; McFarland, E. W. *Nanotechnology* **2010**, *21*, 225708−225716.
(28) Ferrari, A. C. *Solid State Commun.* **2007**, *143*, 47−57.
(29) Ibusuki, T.; Kojima, S.; Kitakami, O.; Shimada, Y. *IEEE Trans. Magn.* **2001**, *37*, 2223−2225.
(30) Taylor, A.; Krupskaya, Y.; Krämer, K.; Füssel, S.; Klingeler, R.; Büchner, B.; Wirth, M. P. *Carbon* **2010**, *48*, 2327−2334.
(31) Shi, C. X.; Cong, H. T. *J. Appl. Phys.* **2008**, *104* (034307), 1−5.
(32) Narayanan, T. N.; Shaijumon, M. M.; Ajayan, P. M.; Anantharaman, M. R. *Nanoscale Res. Lett.* **2009**, *5*, 164−168.
(33) Niederberger, M.; Pinna, N. *Metal oxide nanoparticles in organic solvents*; Springer: London, 2009.
(34) Kittel, C. *Introduction to solid state physics*; John Wiley & Sons:, Hoboken, NJ, 2004.
(35) Andrä, W.; Nowak, H. *Magnetism in Medicine*; Wiley-VCH: Weinheim, Germany, 2007.
(36) Kumar, C. *Nanomaterials for Cancer Therapy*; Wiley-VCH: Weinheim, Germany, 2006.
(37) Krupskaya, Y.; Mahn, C.; Parameswaran, A.; Taylor, A.; Krämer, K.; Hampel, S.; Leonhardt, A.; Ritschel, M.; Büchner, B.; Klingeler, R. *J. Magn. Magn. Mater.* **2009**, *321*, 4067−4071.
(38) El-Gendy, A. A.; Ibrahim, E. M. M.; Khavrus, V. O.; Krupskaya, Y.; Hampel, S.; Leonhardt, A.; Büchner, B.; Klingeler, R. *Carbon* **2009**, *47*, 2821−2828.
(39) Kallumadil, M.; Tada, M.; Nakagawa, T.; Abe, M.; Southern, P.; Pankhurst, Q. A. *J. Magn. Magn. Mater.* **2009**, *321* (10), 1509−1513.
(40) Lukanov, P.; Anuganti, V. K.; Krupskaya, Y.; Galibert, A.; Soula, B.; Tilmaciu, C.; Velders, A. H.; Klingeler, R.; Büchner, B.; Flahaut, E. *Adv. Funct. Mater.* **2011**, *21*, 3583−3588.
(41) Warner, J. H.; Rümmeli, M. H.; Gemming, T.; Büchner, B; Briggs, G. A. D. *Nano Lett.* **2009**, *9*, 102−106.